

# Low-dimensional dynamics of near-wall turbulence

By Javier Jiménez<sup>†</sup> AND Mark Simens<sup>‡</sup>

## 1. Introduction

Wall-bounded turbulent shear flows are perhaps the last area in ‘classical’ incompressible turbulence in which there still are open questions about basic physical mechanisms. There are two competing conceptual models. In the first one, wall turbulence is just a modification of ordinary shear turbulence occurring when the latter is a near wall, and is therefore dependent on the prior existence of an outside turbulent flow. In the second, it is an essentially different phenomenon which coexists with the outer flow and merges into it when the distance from the wall is large enough.

Jiménez (1999) took the latter view and argued that the dynamics of near-wall turbulence is essentially different from the Kolmogorov (1941) mechanism. While the latter is fundamentally isotropic and the energy is dissipated locally by cascading to smaller length scales, wall-bounded flows are intrinsically inhomogeneous and anisotropic, and a substantial part of their energy diffuses from the wall into the outer flow, increasing, rather than decreasing, its length scales in the process.

In this paper we examine the dynamics of the structures of the viscous and buffer layers in very simplified situations in which their interaction with the outer flow is severely restricted. Even natural flows scale in this region approximately in wall units, defined in terms of the kinematic viscosity  $\nu$  and of the friction velocity  $u_\tau = (\nu \partial_y U)^{1/2}$ , where  $U$  is the mean velocity profile. In that approximation, and if we admit that near-wall turbulence is not a just a modification by the wall of the outside turbulent flow, only local quantities such as dimensionless distance to the wall,  $y^+ = u_\tau y / \nu$ , should matter, while global parameters such as the Reynolds number of the flow should be irrelevant.

In the reduced systems considered here, the outer flow is effectively removed, and the scaling in wall variables should be strict. No bulk Reynolds number may be relevant because no bulk turbulent flow exists. Since the local wall-normal Reynolds numbers are low, we may expect quasi-laminar structures whose behavior can be understood deterministically. In this sense this region corresponds to the Kolmogorov viscous range of isotropic turbulence, but we will see that, while the latter is a sink for the energy cascading from the larger scales, the structures studied here are not only self-sustaining, but actually export energy to the rest of the flow.

The organization of this paper is as follows. The energy balance is briefly examined in the next section. The wall region and the numerical experiments undertaken to isolated it are described next. The results are then discussed, with emphasis on the low-dimensional behavior of the structures in the simplified flows and on how they evolve into a fully turbulent flow once the constraints are removed.

<sup>†</sup> Also at U. Politécnica de Madrid

<sup>‡</sup> U. Politécnica de Madrid and U. Twente

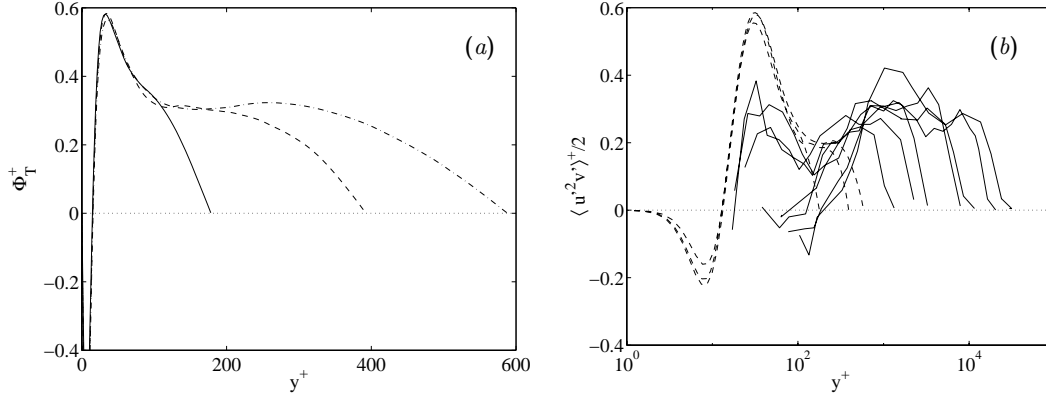


FIGURE 1. Spatial flux of turbulent energy in wall bounded flows, normalized by  $u_\tau^3$ . (a) Total flux computed from integrating Eq. (2.1) in numerical plane channels. —,  $Re_\tau = 180$ , from Kim, Moin & Moser (1987); ----,  $Re_\tau = 395$ ; - · - ·,  $Re_\tau = 590$ , from Moser, Kim & Mansour (1999). (b) Flux of streamwise turbulent fluctuations. The dashed lines are the three channels in (a). The solid ones are boundary layers from Fernholz & Finley (1996).  $Re_\tau \approx 1,200 - 3 \times 10^4$ .

## 2. The balance of turbulent energy

One of the reasons suggesting that the near-wall region is quasi-autonomous, independent of the outer flow, is the behavior of the kinetic energy fluxes as a function of the distance  $y$  to the wall. Consider a streamwise-homogeneous flow, such as a turbulent pipe, and separate the velocity into its mean value and fluctuations. We can write the evolution equation for the mean turbulent kinetic energy,  $K = \langle u'^2 + v'^2 + w'^2 \rangle / 2$ ,

$$\partial_y \Phi_T = -\langle u'v' \rangle \partial_y U - \varepsilon + \nu \partial_{yy} K. \quad (2.1)$$

where  $u'$ ,  $v'$ , and  $w'$  are the streamwise, wall-normal, and spanwise velocity fluctuations, and  $\langle \rangle$  stands for averaging over time and over the two homogeneous coordinates parallel to the wall. The first term in the right-hand side is the production of turbulent energy by the interaction between the mean shear and the Reynolds stresses; the last one is the large-scale viscous diffusion of the kinetic energy, which can be neglected everywhere except in the viscous sublayer, and  $\varepsilon$  is the dissipation by the small scales  $\nu \langle |\nabla \mathbf{u}|^2 \rangle$ . The balance of these three terms is compensated in the left-hand side by the divergence of the spatial energy flux

$$\Phi_T = \frac{1}{2} \langle v'(u'^2 + v'^2 + w'^2) \rangle + \langle v'p' \rangle, \quad (2.2)$$

where  $p'$  are the pressure fluctuations.

It is generally agreed that production and dissipation are approximately in balance across the logarithmic layer (Townsend 1976), implying that the energy flux  $\Phi_T$  should be approximately constant in that region. This is seen to be roughly true in Fig. 1(a), which contains data from three numerical channels at moderate Reynolds numbers. The flux is roughly constant and positive in an intermediate region, showing that energy flows away from the wall. Its positive slope near the wall, on the other hand, implies a local excess of energy production. Part of that extra energy diffuses into the wall, but the rest flows through the logarithmic layer into the outer flow where dissipation is dominant. In this sense, the wall provides the power needed to maintain turbulence in the outer region.

It is, unfortunately, difficult to measure all the terms of the energy equation in experimental flows, and there are no data equivalent to those in Fig. 1(a) for higher Reynolds numbers. Some parts of  $\Phi_T$  have, however, been measured and can be used to check how representative are the numerical results. This is done in Fig. 1(b), which shows the triple product  $\langle u'^2 v' \rangle / 2$ , which is the main contribution to (2.2). The figure includes the numerical channels of Fig. 1(a) and experimental boundary layers at much higher Reynolds numbers. Notwithstanding the uncertainties in the experimental data, especially near the wall where the probe lengths are comparable to the wall distance, both sets of measurements coincide where they overlap, giving some confidence on the interpretation of the numerics.

The picture suggested is that there is an energy-producing region near the wall ( $y^+ < 50$ ) which exports some of its turbulent energy across the logarithmic region into the outer flow.

Both the spatial and the Kolmogorov cascades are present in wall flows. It is difficult to compare their magnitude since  $\Phi_T$ , which is an energy flux per unit area, has different units from  $\varepsilon$ , which is an energy flux per unit volume. We can, however, form a length from the two quantities,  $\lambda_T = \Phi_T / \varepsilon$ , which is the thickness of the layer over which the Kolmogorov cascade would be able to process all the energy provided by the spatial flux. It follows from Fig. 1(a), and from the logarithmic-layer estimate  $\varepsilon \approx u_\tau^2 \partial_y U = u_\tau^3 / \kappa y$ , where  $\kappa \approx 0.4$  is the Kármán constant, that  $\lambda_T \approx 0.15y$ . The turbulent energy being exported across a plane parallel to the wall in the logarithmic region is equivalent to the dissipation in the top 15% of the layer bounded by the plane and the wall.

### 3. The near-wall region

Because of this influence on the global energy balance of the flow and, consequently, on the magnitude of the wall drag, the region below  $y^+ \approx 100$  has been the subject of intensive study.

Its dominant structures are streamwise velocity streaks and quasi-streamwise vortices. The former are an irregular array of long ( $x^+ \approx 1000$ ) sinuous alternating streamwise jets superimposed on the mean shear, with an average spanwise separation shown by Smith & Metzler (1983) to be  $z^+ \approx 100$ . At the spanwise locations where the jets point forward, the wall shear is higher than the average, while the opposite is true for the ‘low velocity’ streaks where the jets point backwards. The quasi-streamwise vortices are slightly tilted away from the wall, and each one stays in the near-wall region only for  $x^+ \approx 200$  (Jeong *et al.*, 1997). Several vortices are associated with each streak, with a longitudinal spacing of the order of  $x^+ \approx 400$  (Jiménez & Moin, 1991), and most of them merge into disorganized vorticity after leaving the immediate wall neighborhood (Robinson, 1991).

It was proposed by Kim, Kline & Reynolds (1971) that streaks and vortices are part of a cycle in which the vortices are the results of an instability of the streaks, while the vortices cause the streaks by advecting the mean velocity gradient (Swearingen & Blackwelder, 1987). While there is general agreement on the latter part of the cycle, the mechanism by which the vortices are generated is less clear. It was shown by Jiménez & Pinelli (1999) that disturbing the streaks inhibits the formation of the vortices, resulting in the eventual decay of the turbulence, and that the region in which the disturbances are effective is restricted to between  $y^+ \approx 10$  and  $y^+ \approx 60$ . That paper contains a more

complete summary of the different models for the near-wall region in natural turbulent flows and should be consulted for additional references.

A slightly different point of view is that the cycle is organized around a nonlinear traveling wave, a fixed point in phase space, which would represent a permanently disturbed streak. This is actually not too different from the previous instability model, which essentially assumes that the undisturbed streak is a fixed point, and that the cycle is an approximation to a homoclinic orbit running through it. Candidate nonlinear waves have been computed by Waleffe (1998) and others, and identified as part of a particular path to turbulent transition by Toh & Itano (1999). Finally, reduced models based on this approach have been formulated by Waleffe (1997).

A difficulty with most of these studies, with the possible exception of the one by Toh & Itano (1999), is that there is no clear connection between the object being studied and full-scale turbulence. What we intend in this paper is to show that a turbulent flow can be continuously modified into one of those reduced objects while still remaining identifiably turbulent.

A way of doing this was proposed by Jiménez & Moin (1991), who substituted a full turbulent channel by an array of identical computational boxes, periodic in the streamwise and spanwise directions  $x$  and  $z$ , while retaining its full wall-normal extent. The idea was to substitute the complexity of all the mutually interacting turbulent units near the wall by a ‘crystal’ of identical structures executing synchronously the hypothetical turbulence regeneration cycle. The ‘unit cell’ of the crystal was adjusted to the smallest dimension that would maintain turbulence, which turned out to contain a single wavelength of a wavy low-velocity streak and a pair of quasi-streamwise vortices. These structures went through a complex cycle which was still difficult to analyze, while the statistics of the near-wall fluctuations were essentially identical to those of fully developed channels. This ‘minimal’ system has often been used as a surrogate for real wall turbulence, and most of the reduced models mentioned above actually refer to it.

The previous experiment eliminates the possibility that wall turbulence requires the interaction between neighboring wall structures, but says nothing about the importance of its interaction with the core flow. A step in clarifying that question was taken by Jiménez & Pinelli (1999), who eliminated the vorticity fluctuation in the outer flow of a numerical channel by using a numerical filter which acts as a variable viscosity which is low near the wall and increases away from it. They were able to show that the wall cycle was ‘autonomous’ in the sense that it could run independently of the outer flow as long as it was not disturbed below  $y^+ \approx 60$ . Again the statistics were similar, although no longer identical, to those of full turbulence.

In this paper we describe the results of simulations which are both ‘minimal’, in the sense that their wall-parallel size is small enough to contain a single copy of each structure, and autonomous in the sense that they have no turbulent external flow.

#### **4. The numerical experiments**

The numerical scheme used for the simulations is similar to the one described by Jiménez & Pinelli (1999). The Navier-Stokes equations are integrated in the form of evolution equations for the wall-normal vorticity  $\omega_y$  and for  $\phi = \nabla^2 v$ , using a pseudospectral code with Fourier expansions in the two wall-parallel directions and Chebychev polynomials in  $y$ , as in Kim, Moin & Moser (1987). At each time step the right-hand sides of

the two evolution equations are multiplied by a damping filter

$$F(y) = 1 \quad \text{if } y \leq \delta_1, \quad F(y) = F_0 < 1 \quad \text{if } y \geq \delta_2, \quad (4.1)$$

with the two limits connected smoothly by a cubic spline. In all of our experiments  $\delta_2 \approx 1.5 \delta_1$ . Because the filter is applied at every time step, it is very effective in damping the vorticity fluctuations, and it was shown by Jiménez & Pinelli (1999) that the complete suppression of the fluctuations only requires that  $1 - F \gg \Delta t^+$ , where  $\Delta t$  is the computational time step. In practice we use  $F_0 = 0.95$ , and the damping is effective approximately midway between  $\delta_1$  and  $\delta_2$ . The evolution equations for the  $(0, 0)$  Fourier modes of  $u$  and  $w$ , which cannot be expressed in terms of  $\omega_y$  and  $\phi$ , are not modified by the filter.

The flow is integrated at constant mass flux in a channel, periodic in  $x$  and  $z$ . No-slip impermeable boundary conditions are imposed at  $y = 0$  and  $y = 2$ . The volumetric flux is adjusted so that the Reynolds number of an undamped turbulent channel would have been  $Re_\tau \approx 200$ . Because there are no Reynolds stresses in the region in which the filter is active, the mean velocity profile is there parabolic (see Fig. 2*a*), sequestering much of the total mass flux, and the final Reynolds number is usually closer to  $Re_\tau \approx 120$ . As previously mentioned, however, such Reynolds numbers are irrelevant because no turbulent flow extends to the far wall. The relevant turbulent Reynolds number is the height of the damping function  $\delta_1^+ = u_\tau \delta_1 / \nu$ , which determines the size of the largest turbulent scales.

It was stated by Jiménez & Pinelli (1999) that the damping function was approximately equivalent to a viscosity proportional to the velocity instead of to its Laplacian. This is only partly correct. While the effect of (4.1) is equivalent to a zeroth-order viscosity for the two evolution variables, the velocities are obtained from them using the definition of the vorticity and the continuity equation, and potential velocity fluctuations penetrate into the damped region. Even the vorticity fluctuations are not completely suppressed since only  $\omega_y$  is directly damped while the other two vorticity components have to satisfy the solenoidality condition (i.e. the vortex lines have to close).

The flow below  $y = \delta_1$  satisfies the unmodified Navier-Stokes equations. It was shown by Jiménez & Pinelli (1999) that the mean velocity and the fluctuations in that layer were very similar to those in regular channels even when  $\delta_1^+ \approx 50$ . Those results were obtained in a computational box whose length and width were much larger than the filter height and which was essentially turbulent. We will present here results for much smaller boxes, some of which contain very ordered flows in which there are no temporal chaotic fluctuations to smear the effect of the individual structures and whose mean profiles, therefore, differ substantially from those of natural turbulent channels. Some examples are given in Fig. 2.

The three boxes used for that figure contain respectively a fixed point in phase space, corresponding to a permanent traveling wave, a two-frequency torus, and a mildly chaotic flow. All of them are too short to sustain a strongly chaotic flow that could be interpreted as turbulence, and although they are wider than the mean distance between streaks in natural turbulence, each of them is shown by direct visualization to contain a single low-velocity streak (see Fig. 6 below).

The mean velocity profiles show a plateau which can be interpreted as an abortive logarithmic layer, although in this case the velocity decreases slightly before joining the parabolic profile of the irrotational region. The local maxima present in the vorticity profiles below the filter height are real, and correspond to individual features which,

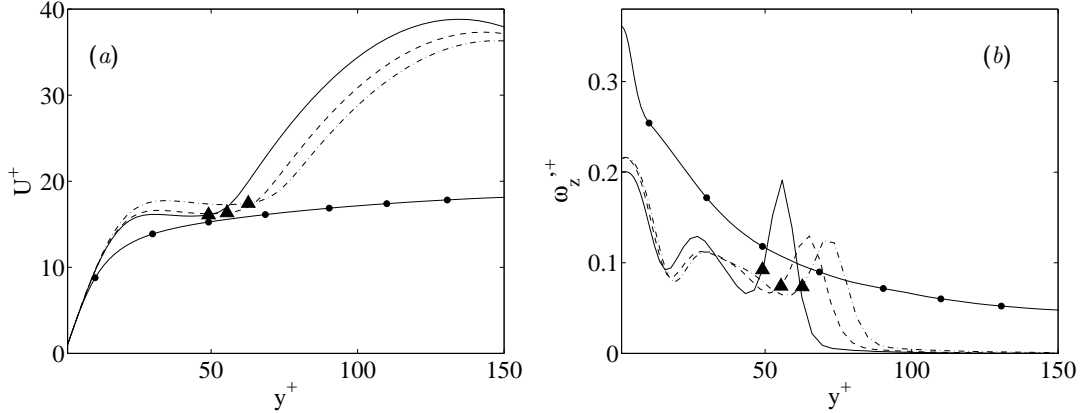


FIGURE 2. Mean profiles for three autonomous computational boxes. —,  $L_x = 145$ ,  $L_z = 180$ ,  $\delta_1^+ = 49$ ,  $\delta_2^+ = 71$ ; ---,  $L_x = 150$ ,  $L_z = 185$ ,  $\delta_1^+ = 55$ ,  $\delta_2^+ = 86$ ; - · - ·,  $L_x = 155$ ,  $L_z = 190$ ,  $\delta_1^+ = 63$ ,  $\delta_2^+ = 94$ . The line with symbols is the full channel from Kim, Moin & Moser (1987), included for comparison. The solid triangle in each profile marks the lower limit of the damping function (4.1). (a) Mean velocity. (b) Fluctuation intensity of the spanwise vorticity.

in these relatively ordered flows, stay at a constant distance from the wall instead of wandering chaotically as in natural turbulence, but the strong peaks located just above  $\delta_1$  are artifacts of the damping filter. They mark the reconnection or the vortex lines after they are truncated by the damping, as described above.

Two types of numerical boxes were studied, both of which had widths  $L_z^+ \approx 180$  when the filter height was set near its minimal value of  $\delta_1^+ \approx 50$ . The longer ones, which contain two streamwise copies of the basic structure, have  $L_x^+ \approx 300$  and were run using  $42 \times 97 \times 31$  spectral modes in the streamwise, wall-normal, and spanwise directions after dealiasing. The shorter boxes, which are only half as long in the streamwise direction, were run using 20 streamwise modes. The resolution,  $\Delta x^+ \approx 7$ ,  $\Delta z^+ \approx 6$ , with the first collocation point at  $y^+ \approx 0.07$ , is therefore excellent.

As the filter height is raised, the effective  $Re_\tau$  increases to values closer to 180, and the grid spacing increases by about 50% in wall units. The resolution of those simulations, which are essentially full minimal channels, is therefore correspondingly worse but still adequate.

## 5. Results

In a first series of numerical experiments, the vertical filter was set to  $\delta_1^+ \approx 50$ , and the wall-parallel box size was changed. The simulations were then run until they achieved statistically steady state. Each simulation was initialized from a statistically converged instantaneous field from another box of roughly similar dimensions. The transition from long to short boxes was made by zeroing all of the odd streamwise Fourier coefficients of one of the former, thus essentially averaging the two wavelengths contained in it. Because the basin of attraction of nontrivial solution in some of the tighter boxes is fairly small, this initialization procedure was essential for their survival.

The boxes discussed here are those which turn out to be small enough to contain recognizable simple flow structures and a single low-velocity streak in the spanwise direction. For two selected box lengths, the height of the filter was varied systematically. As the

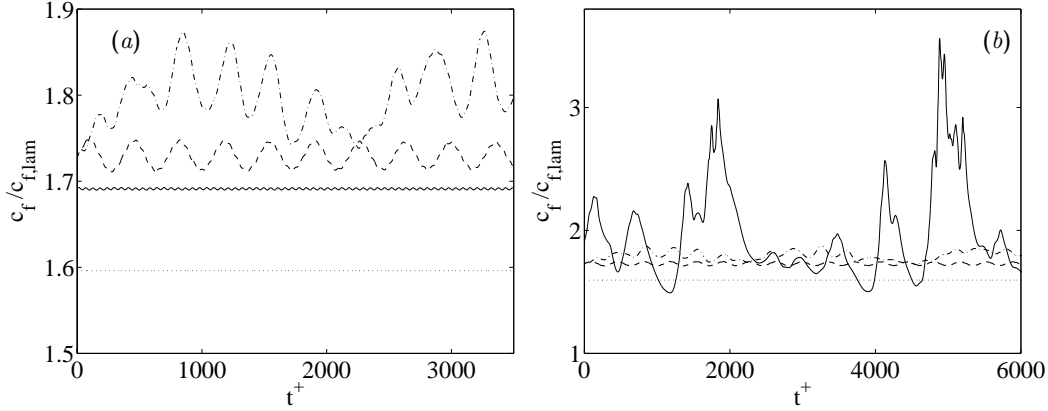


FIGURE 3. Time evolution of the instantaneous friction coefficient. (a)  $\cdots$ ,  $L_x^+ = 145$ ,  $\delta_1^+ = 49$ ;  $\text{—}$ ,  $L_x^+ = 150$ ,  $\delta_1^+ = 52$ ;  $\text{- - -}$ ,  $L_x^+ = 152$ ,  $\delta_1^+ = 55$ ;  $\text{- \cdot -}$ ,  $L_x^+ = 154$ ,  $\delta_1^+ = 63$ . (b) Symbols are as in (a) except for,  $\text{—}$ ,  $L_x^+ = 161$ ,  $\delta_1^+ = 78$ . Note the difference in scale between the two figures.

filter height increased, especially as it was made comparable to the channel half-height, the extent of the parabolic part of the profile decreased and the effective  $Re_\tau$  increased. Although some efforts were made to compensate this effect by changing the length and width of the computational boxes, there is some systematic variation of both quantities with the filter height when expressed in wall units.

The time evolution of the flow was characterized in two different ways. The first one is the evolution of the instantaneous skin friction, defined as the gradient at the wall of the plane-averaged streamwise velocity. Because of the ambiguities regarding dimensional bulk variables, only the fluctuations relative to its own mean make sense

$$c_f^+ = \frac{\partial_y \bar{u}}{\partial_y U}, \quad (5.1)$$

where the overline stands for instantaneous averaging over wall-parallel planes and  $U$  is the long-time average of  $\bar{u}$ .

Some representative time histories are shown in Fig. 3. They have been normalized with the skin friction of a parabolic laminar profile with the same mass flux to separate them vertically for visual clarity, but we have seen that the different levels of the average wall friction have no physical significance. All of the simulations in Fig. 3 are ‘short’ boxes containing a single wavelength of the low-velocity streak. For the lowest filter height, the flow is a permanent wave which moves with a celerity  $u_c^+ \approx 15$ . This case corresponds to the solid line in the profiles in Fig. 2(a), and the advection velocity is very close to that of the plateau in the mean velocity profile. The next two filter heights result in two-frequency tori, with a short period  $T^+ \approx 60$  and a long one  $T^+ \approx 400$ . The relative importance of both periods switches with the filter height. While for  $\delta_1^+ = 52$  the long period is only a weak modulation of the short one, invisible at the scale of Fig. 3, the opposite is true when  $\delta_1^+ = 55$ .

As the filter is raised further, the flow becomes chaotic, with the longest period of the tori acting now as a dominant fast frequency. Finally, for  $\delta_1^+ > 70$ , intermittent bursts appear which are typical of fully developed turbulent flows and whose amplitude is substantially higher than in any of the three other cases (Fig. 3b). The shortest bursting

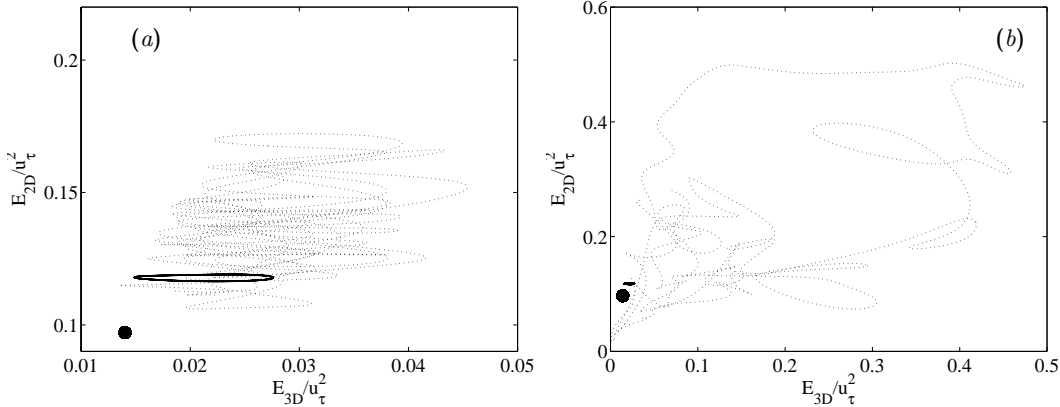


FIGURE 4. Time evolution of the fluctuating energies. (a)  $\bullet$ ,  $L_x^+ = 145$ ,  $\delta_1^+ = 49$ ;  $\text{—}$ ,  $L_x^+ = 150$ ,  $\delta_1^+ = 52$ ;  $\cdots\cdots$ ,  $L_x^+ = 154$ ,  $\delta_1^+ = 63$ . (b) Symbols are as in (a) except for,  $\cdots\cdots$ ,  $L_x^+ = 161$ ,  $\delta_1^+ = 78$ . Note the different scales of the two figures, which result in the weakly-modulated cycle in (a) being reduced to a short horizontal dash in (b).

events are roughly of the same length as the long period of the tori, while the longest ones are two or three times longer. These times are comparable to those identified for individual bursts in minimal channels by Jiménez & Moin (1991). The present boxes are actually too short to maintain bursting turbulence, which is metastable. The velocity fluctuations become very weak in the dips of the history of the skin friction until one of them fails to regenerate and the flow laminarizes completely.

Figure 4 shows the same data in a different representation introduced by Toh & Itano (1999). Orbits are drawn in terms of the two-dimensional and three-dimensional energy of the wall-normal velocity fluctuations. The two-dimensional energy is

$$E_{2D} = \frac{1}{H} \int_0^H \langle v_{2D}^2 \rangle dy, \quad (5.2)$$

where  $v_{2D}(y, z, t)$  is the streamwise average of the fluctuation of  $v$  and therefore measures the intensity of objects which are long in the streamwise direction, essentially streaks. The three-dimensional energy is similarly defined for the remaining  $v$  fluctuations,  $v_{3D} = v - v_{2D}$ , and measures deviations from streamwise uniformity. In this representation the permanent wave is represented by a single point, while the weakly modulated torus of Fig. 3(a) appears almost as a limit cycle, wide in the sense of the three-dimensional energy but narrow in the two-dimensional one. The examination of this cycle as well as of the orbits corresponding to other cases shows that the skin friction correlates with the magnitude of the two-dimensional energy and, therefore, of the intensity of the streak, while the faster oscillations of the three-dimensional energy do not affect it strongly.

Figure 4(b) underscores the different range of amplitudes of the simple tori or chaotic flows, which are obtained for low filter heights, and of the bursts of the deeper channels, but it also suggests that the simplification process consists of damping the large bursting excursions, while the low-activity periods of the deeper flows share with the constrained systems the same region of the energy space.

Similar behaviors are found for the longer boxes, which contain at least two wavelength of the wavy streak. A summary of cases is found in Fig. 5(a), which classifies the different experiments in terms of their temporal behavior. Note the narrow range of filter heights

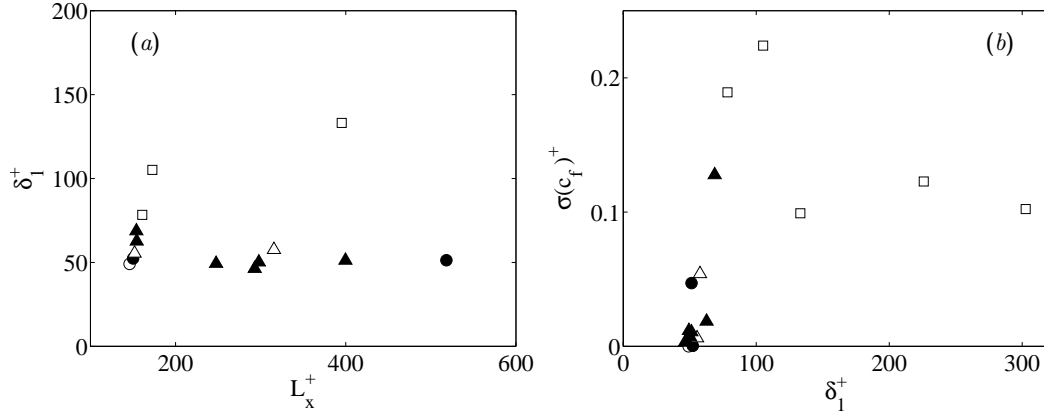


FIGURE 5. (a) Classification of the evolution of the different computational experiments, as a function of the box length  $L_x^+$ , and of the filter height  $\delta_1^+$ . (b) Root mean squared temporal variation of the plane-averaged wall friction.  $\circ$ , permanent wave;  $\bullet$ , cycle or weak torus;  $\triangle$ , simple torus;  $\blacktriangle$ , complex torus or chaos;  $\square$ , bursting turbulence.

which result in time evolutions which are not fully turbulent, but also that the bursting appears as a natural evolution of the weakly chaotic flows. In the longer boxes the bursting turbulence is self-sustaining and does not decay spontaneously.

The amplitude of the skin friction fluctuations, normalized as in (5.1), is given in Fig. 5(b). The bifurcation parameter that collapses the different experiments is  $\delta_1^+$ , and the fluctuations increase quickly above a minimum threshold  $\delta_1^+ \approx 50$ . There are two branches in this figure, representing respectively the long and the short boxes. The steeper branch consists of short boxes, and the lower fluctuation amplitude of the long ones reflects the fact that not all the structures burst simultaneously and that the amplitudes measured in the long boxes represent an average of bursting and quiescent structures.

A three-dimensional representation of the flow field in one of the longer boxes is shown in Fig. 6(a). It shows a low-velocity streak with two waves, associated to each of which there is a pair of quasi-streamwise vortices. During the turbulent cycle the amplitude of the lateral displacement of the streak grows and wanes, and so do the vortices, but the streak is never uniformly straight. Careful tracing of vortex lines, although generally complicated, proves that the streak and the vortices are not independent structures, but different aspects of the same one. The single permanent wave mentioned above when discussing the time histories is shown in Fig. 6(b). It should be emphasized that this wave is both permanent, moving at a constant velocity without change of shape, and autonomous, in the sense that there are no vorticity fluctuations in the numerical box except those seen in the figure and that it has been derived from a fully turbulent flow by a continuous set of transformations in which its statistical properties are either maintained or change smoothly. It is the best representation that we have up to now of the elemental ‘engine’ that powers near-wall turbulence.

Figures 6(a) and 6(b) are qualitatively very similar to the traveling waves obtained in Waleffe (1998) and to the structures deduced from larger channels by Jiménez & Moin (1991) and Jiménez & Pinelli (1999), as well as to the saddle point identified by Toh & Itano (1999).

Careful observation of the differences between computer animations of these and of deeper boxes suggests the root of the increased complexity of the latter. As the streak goes

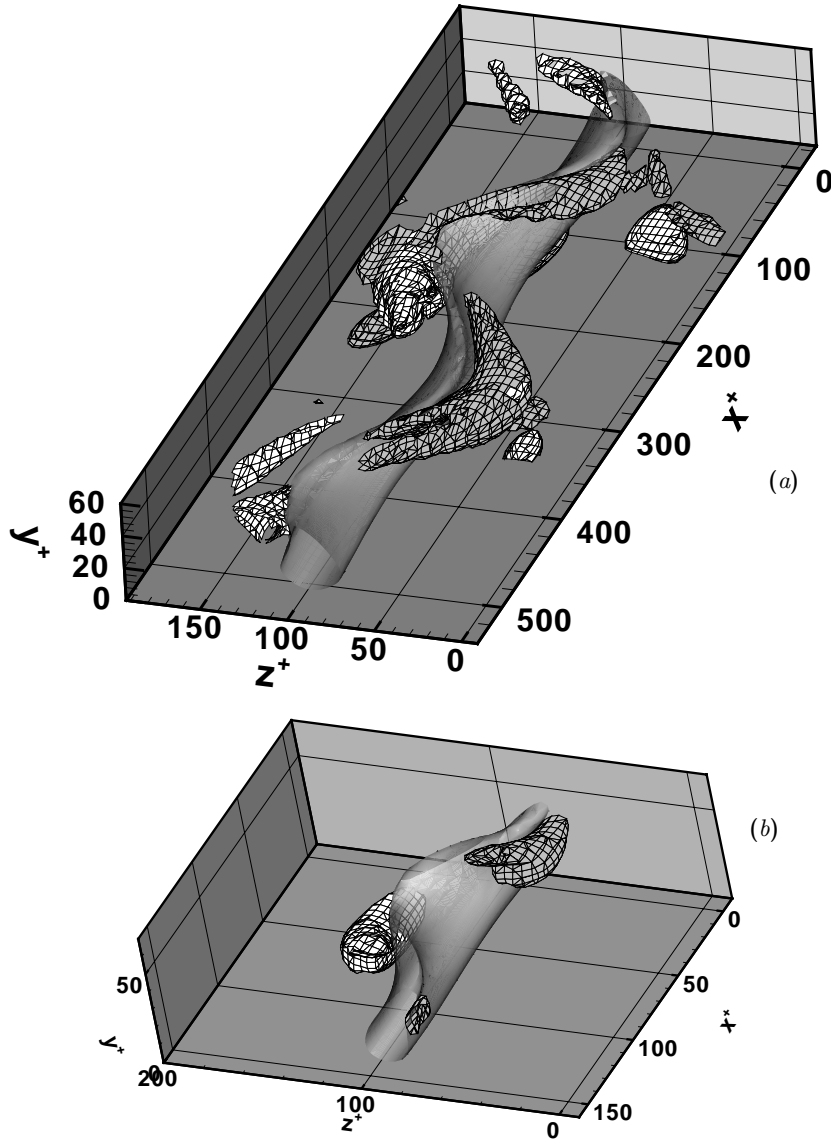


FIGURE 6. Three-dimensional representations of two of the flows discussed in the text. The shaded surface is in both cases  $u'^+ = -3.5$ . The meshed objects are  $\omega_x^+ = \pm 0.18$ . The darker quasi-streamwise vortices are negative, so that the net effect of the vortex system is to induce a positive updraft along the low-velocity streak. The flow is from top-right to bottom-left. (a) is a regular cycle with  $L_x^+ = 520$ ,  $\delta_1^+ = 51$ . (b) is the steady wave in Figs. 3 and 4.

through the cycle, it ejects some vorticity into the outer flow, essentially as a small vortex hairpin. In full-depth flows this vorticity evolves, becomes disorganized, and eventually modifies the next cycle of the streak. In autonomous flows the vorticity is damped by the filter as soon as it is ejected, and this randomizing mechanism is not present. The threshold filter height at which bursting first appears is that for which the vortices are

just allowed to move far enough from the wall to cross over the top of the streak and interact with one another.

## 6. Conclusions

We have shown that simple low-dimensional systems can be obtained from fully turbulent channels by a continuous set of transformations, the most important of which is the restriction of the distance from the wall at which the quasi-streamwise vortices are allowed to move.

The simplest solution identified in this way is a permanent traveling wave, similar to those found by other investigators in related flows. As the vertical constraints on the system are relaxed, this wave bifurcates into either a limit cycle or a two-frequency torus, depending on the parameters. The longest of the two periods of the torus evolves into the bursts of full-scale turbulence when the vertical restriction is further removed.

The critical bifurcation filter height is  $\delta_1^+ \approx 50$ , and the range of heights in which the bifurcation occurs is very narrow, with the flow becoming essentially turbulent for  $\delta_1^+ \approx 70$ . The bifurcation mechanism was identified visually as the interaction, across the top of the low-velocity streak, of the two counter-rotating vortices.

Even in the very short boxes used in these simulations, the only streamwise coherent structure is the low-velocity streak. The quasi-streamwise vortices, their associated wall-normal velocities, and the resulting high-shear regions near the wall are all discontinuous along the box length.

M. S. was supported in part by grant CT98-0175 of the TMR program.

## REFERENCES

- FERNHOLZ, H. H., & FINLEY, P. J. 1996 The incompressible zero-pressure-gradient turbulent boundary layer: an assessment of the data. *Prog. Aerospace Sci.* **32**, 245-311.
- JEONG, J., HUSSAIN, F., SCHOPPA, W. & KIM, J. 1997 Coherent structures near the wall in a turbulent channel flow. *J. Fluid Mech.* **332**, 185-214.
- JIMÉNEZ, J. 1999 The physics of wall turbulence, *Physica A.* **263**, 252-262.
- JIMÉNEZ, J. & MOIN, P. 1991 The minimal flow unit in near wall turbulence. *J. Fluid Mech.* **225**, 221-240.
- JIMÉNEZ, J. & PINELLI, A. 1999 The autonomous cycle of near wall turbulence. *J. Fluid Mech.* **389**, 335-359.
- KIM, H. T., KLINE, S. J. & REYNOLDS, W. C. 1971 The production of turbulence near a smooth wall in a turbulent boundary layers. *J. Fluid Mech.* **50**, 133-160.
- KIM, J., MOIN, P. & MOSER, R. 1987 Turbulence statistics in fully developed channel flow at low Reynolds number. *J. Fluid Mech.* **177**, 133-166.
- KOLMOGOROV, A. N. 1941 The local structure of turbulence in incompressible viscous fluids at very large Reynolds numbers. *Dokl. Akad. Nauk. SSSR*, **30**, 301-305. Reprinted in *Proc. R. Soc. London A.* **434**, 9-13 (1991).
- MOSER, R., KIM, J. & MANSOUR, N. N. 1999 Direct numerical simulation of a turbulent channel flow up to  $Re_\tau = 590$ . *Phys. Fluids.* **11**, 943-945.
- ROBINSON, S. K. 1991 Coherent motions in the turbulent boundary layer. *Ann. Rev. Fluid Mech.* **23**, 601-639.

- SMITH, C. R. & METZLER, S. P. 1983 The characteristics of low speed streaks in the near wall region of a turbulent boundary layer. *J. Fluid Mech.* **129**, 27-54.
- SWEARINGEN, J. D. & BLACKWELDER, R. F. 1987 The growth and breakdown of streamwise vortices in the presence of a wall. *J. Fluid Mech.* **182**, 255-290.
- TOH, S. & ITANO, T. 1999 Low-dimensional dynamics embedded in a plane Poiseuille flow turbulence. Traveling-wave solution is a saddle point? Preprint *physics/9905012*.
- TOWNSEND, A. A. 1976 *The structure of turbulent shear flow*. Cambridge U. Press, second edition, pg. 135.
- WALEFFE, F. 1997 On a self-sustaining process in shear flows. *Phys. Fluids.* **9**, 883-900.
- WALEFFE, F. 1998 Three-dimensional coherent states in plane shear flows. *Phys. Rev. Letters.* **81**, 4140-4143.